

Nonlinear optical response in kagome lattice with inversion symmetry breaking

Xiangyang Liu,^{†,‡} Junwen Lai,^{†,‡} Jie Zhan,^{†,‡} Tianye Yu,[‡] Peitao Liu,^{†,‡} Seiji
Yunoki,^{¶,§,||,⊥} Xing-Qiu Chen,^{*,†,‡} and Yan Sun^{*,†,‡}

[†]*School of Materials Science and Engineering, University of Science and Technology of
China, Shenyang 110016, China.*

[‡]*Shenyang National Laboratory for Materials Science, Institute of Metal Research, Chinese
Academy of Sciences, Shenyang 110016, China.*

[¶]*Computational Materials Science Research Team, RIKEN Center for Computational
Science (R-CCS), Hyogo 650-0047, Japan*

[§]*Quantum Computational Science Research Team, RIKEN Center for Quantum Computing
(RQC), Wako, Saitama 351-0198, Japan*

^{||}*Computational Condensed Matter Physics Laboratory, RIKEN Cluster for Pioneering
Research (CPR), Saitama 351-0198, Japan*

[⊥]*Computational Quantum Matter Research Team, RIKEN Center for Emergent Matter
Science (CEMS), Saitama 351-0198, Japan*

E-mail: xingqiu.chen@imr.ac.cn; sunyan@imr.ac.cn

Abstract

The kagome lattice is a fundamental model structure in condensed matter physics and materials science featuring symmetry-protected flat bands, saddle points, and Dirac points. This structure has emerged as an ideal platform for exploring various quantum physics. By combining effective model analysis and first-principles calculations, we

propose that the synergy among inversion symmetry breaking, flat bands, and saddle point-related van Hove singularities within the kagome lattice holds significant potential for generating strong second-order nonlinear optical response. This property provides an inspiring insight into the practical application of the kagome-like materials, which is helpful for a comprehensive understanding of kagome lattice-related physics. Moreover, this work offers an alternative approach for designing materials with strong a second-order nonlinear optical response.

Keywords: distorted kagome lattice, BPVE, shift current, flat bands, saddle points

INTRODUCTION

The kagome lattice, characterized by the geometry of corner-sharing equilateral triangles, is recognized as one of the most intriguing structures in condensed matter physics and materials science. Its electronic structure is notable for the coexistence of the flat bands, saddle point related van Hove singularities (VHSs), and Dirac points. Due to its special lattice and electronic structure, the kagome lattice serves as an ideal model platform for exploring the interplay of electron correlations, topological charges, frustrated magnetism, quantum phase transitions, and strong (or quantized) anomalous transport phenomena.¹⁻⁵

In addition to the aforementioned characteristics, the presence of flat bands and saddle points within the kagome lattice can result in a divergent density of states (DOS). The δ -function in the formula of second-order nonlinear optical conductivity (see Eq. 6) indicates that this property establishes it as a natural platform for strong optical response, owing to the resulting large optical transition response.⁶⁻¹⁸ However, a critical requirement for observing second-order nonlinear optical response is the breaking of inversion symmetry. Fortunately, recent advancements in both experimental and theoretical research have provided several effective strategies to achieve this. These strategies include the synthesis of compounds with distorted kagome lattice,¹⁹⁻²⁴ substrate-induced effects,²⁵⁻²⁹ phase transitions driven by external fields,³⁰⁻³⁵ intercalation or defects,³⁶⁻³⁸ and heterostructure engineering or controlled

layer stacking,^{39,40} among others. With these conditions, we propose a design principle aimed at generating strong nonlinear optical response through the synergistic effect of flat bands, and saddle point related VHSs in the context of two-dimensional (2D) distorted kagome lattice. This work not only expands the scope of the kagome lattice research but also provides a robust principle for designing materials with enhanced nonlinear optical functionalities. By integrating theoretical insights with practical design principles, this study paves the way for manipulating nonlinear optical response in the kagome lattice.

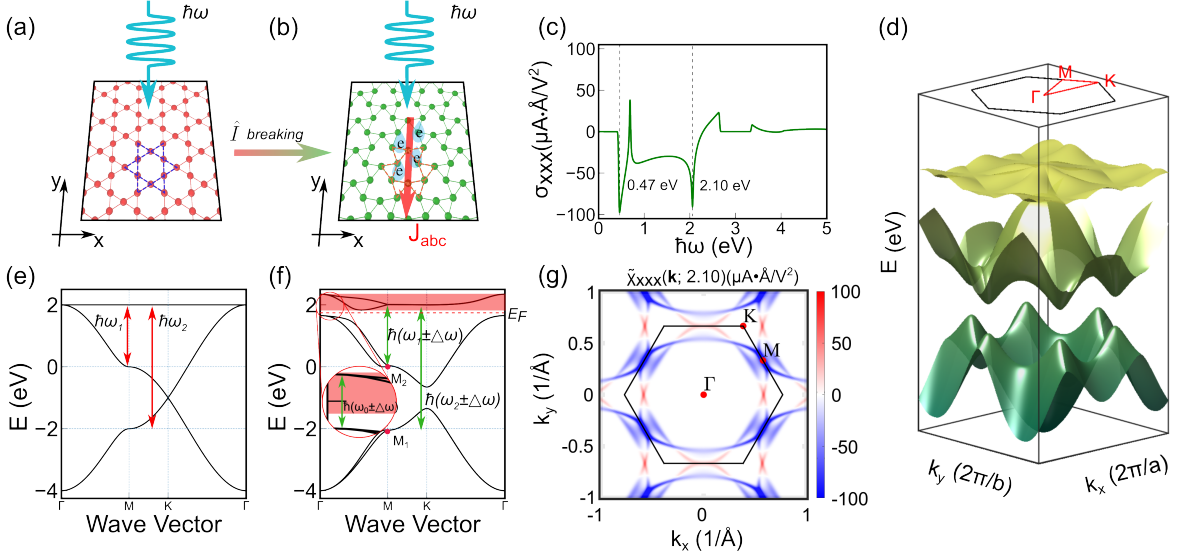


Figure 1: Schematic of second-order nonlinear optical response and band structures of ideal and distorted kagome lattices. (a) A net photocurrent is absent in an ideal kagome lattice with inversion symmetry. (b) A non-zero net photocurrent is allowed in a distorted kagome lattice. (c) Calculated second-order nonlinear optical conductivity for the lattice structure in (b). (d) Energy dispersion for lattice structure (b) over the entire Brillouin zone. (e) Energy dispersion for an ideal kagome lattice. (f) Energy dispersion for a distorted kagome lattice after consideration of SOC and inversion symmetry breaking. (g) Second-order nonlinear optical conductivity density distribution in momentum space with transition energy lying at $\hbar\omega = 2.1$ eV. The parameters $t_1 = -1.0$ eV, $t_2 = 0.0$ eV, and $\lambda_{SOC} = -0.2$ eV were used.

RESULTS AND DISCUSSION

Starting from the conventional kagome lattice depicted in Figure 1a, when considering the nearest electron hopping, the kagome lattice hosts two saddle points at M and one Dirac cone

at K . Owing to the destructive interference of Bloch functions at the nearest-neighbor (NN) sites, the kinetic energy is fully quenched and the top band presents as an infinite effective mass flat band over the entire Brillouin zone (BZ), as illustrated in Figure 1e.^{41–45} Generally, optical transitions from two saddle points to the flat bands, and even the transitions between flat bands and normal bands, can generate a strong optical transition response, which is believed to be a prerequisite for a large second-order nonlinear optical response.

Nevertheless, second-order nonlinear optical response is forbidden by the inversion symmetry within the ideal kagome lattice. To utilize the large optical transition response, we introduce a slight lattice distortion as an example to break the inversion symmetry while preserving the shape of the saddle points and flat bands. To achieve this, one can rotate the adjacent triangles in opposite directions, resulting in a Reuleaux-triangle-shaped lattice configuration, as depicted in Figure 1b. The rotation angle can vary from 0° to 30° , corresponding to a kagome lattice and a coloring-triangular lattice, respectively (see Figure S1a-c). Correspondingly, a six-band effective Hamiltonian is constructed in momentum space is given by.^{43,45}

$$\mathcal{H} = \mathcal{H}^{\text{NN}} \otimes \mathbb{I}_{2 \times 2} + \mathcal{H}^{\text{NNN}} \otimes \mathbb{I}_{2 \times 2} + \mathcal{H}^{\text{SOC}} \otimes \sigma_z, \quad (1)$$

where the first two terms \mathcal{H}^{NN} and \mathcal{H}^{NNN} describe the NN and next NN (NNN) hoppings, respectively. Spin-orbit coupling (SOC) is included here to open the gap between the fourth and fifth bands, which is described as the third term \mathcal{H}^{SOC} . The 3×3 matrices \mathcal{H}^{NN} , \mathcal{H}^{NNN} , and \mathcal{H}^{SOC} are given by

$$\mathcal{H}^{\text{NN}} = t_1 \begin{pmatrix} 0 & c_1 & c_3 \\ c_1^* & 0 & c_2 \\ c_3^* & c_2^* & 0 \end{pmatrix}, \quad (2)$$

$$\mathcal{H}^{\text{NNN}} = t_2 \begin{pmatrix} 0 & b_1 & b_3 \\ b_1^* & 0 & b_2 \\ b_3^* & b_2^* & 0 \end{pmatrix}, \quad (3)$$

and

$$\mathcal{H}^{\text{SOC}} = i\lambda_{\text{SOC}} \begin{pmatrix} 0 & b_1 & -b_3 \\ -b_1^* & 0 & b_2 \\ b_3^* & -b_2^* & 0 \end{pmatrix}, \quad (4)$$

where, $c_1 = e^{i\vec{k}\cdot\frac{\vec{v}_1-\vec{v}_3}{3}} + e^{i\vec{k}\cdot\frac{\vec{v}_3-\vec{v}_2}{3}}$, $c_2 = e^{i\vec{k}\cdot\frac{\vec{v}_2-\vec{v}_1}{3}} + e^{i\vec{k}\cdot\frac{\vec{v}_1-\vec{v}_3}{3}}$, $c_3 = e^{-i\vec{k}\cdot\frac{\vec{v}_3-\vec{v}_2}{3}} + e^{-i\vec{k}\cdot\frac{\vec{v}_2-\vec{v}_1}{3}}$, $b_1 = e^{i\vec{k}\cdot\frac{\vec{v}_2-\vec{v}_1}{3}}$, $b_2 = e^{i\vec{k}\cdot\frac{\vec{v}_3-\vec{v}_2}{3}}$, and $b_3 = e^{i\vec{k}\cdot\frac{\vec{v}_3-\vec{v}_1}{3}}$. Here, \vec{v}_1 and \vec{v}_2 represent the basis vectors of the distorted kagome primitive cell, with \vec{v}_3 defined as $-(\vec{v}_1 + \vec{v}_2)$, while the t_i is the hopping integral (see Figure S2a).

With the given hopping parameters and considering the influence of SOC, the lattice distortion alters the band structure from Figure 1d,f. One can see that although the Dirac cone at K is broken by opening a band gap, two saddle points at M persist, and the wrinkling magnitude $\hbar\Delta\omega$ of flat bands is small. Furthermore, a full band gap emerges between the fourth and fifth bands, and local flat regions form in the third and the fourth bands around the Γ point. As a result, the large optical transition response is maintained after the lattice distortion with inversion symmetry breaking, and a strong second-order nonlinear optical response is expected (see Figure S2b-c). The bulk photovoltaic effect (BPVE) can generate a steady photocurrent with photovoltage above the band gap. According to the current understanding, the shift current is believed to be one of the major origins of the BPVE. Therefore we will mainly focus on the shift current.^{11,44,46-49}

As depicted in Figure 1c, with the chemical potential set between the fourth and fifth bands, two distinct peaks of second-order nonlinear optical conductivity emerge near the photon energies of 0.47 eV and 2.10 eV. After analyzing the band structure in Figure 1f, one can observe that the peak near 0.47 eV ($\hbar(\omega_0 \pm \Delta\omega)$) corresponds to the optical transition between the fourth band and the flat bands near the Γ point, which is indicated by the arrow in the inset. Similarly, the second peak near 2.10 eV ($\hbar(\omega_1 \pm \Delta\omega)$) aligns with the optical transition from the saddle point M_2 to the flat bands. This speculation is further supported by the detailed analysis of the DOS and transition energy isosurfaces in Figure S3.

Since a large optical transition response is only a prerequisite but not a sufficient condition for the strong nonlinear optical response, a large shift current corresponding to the optical transition between the saddle point M_1 and the flat bands does not appear in Figure 1c.

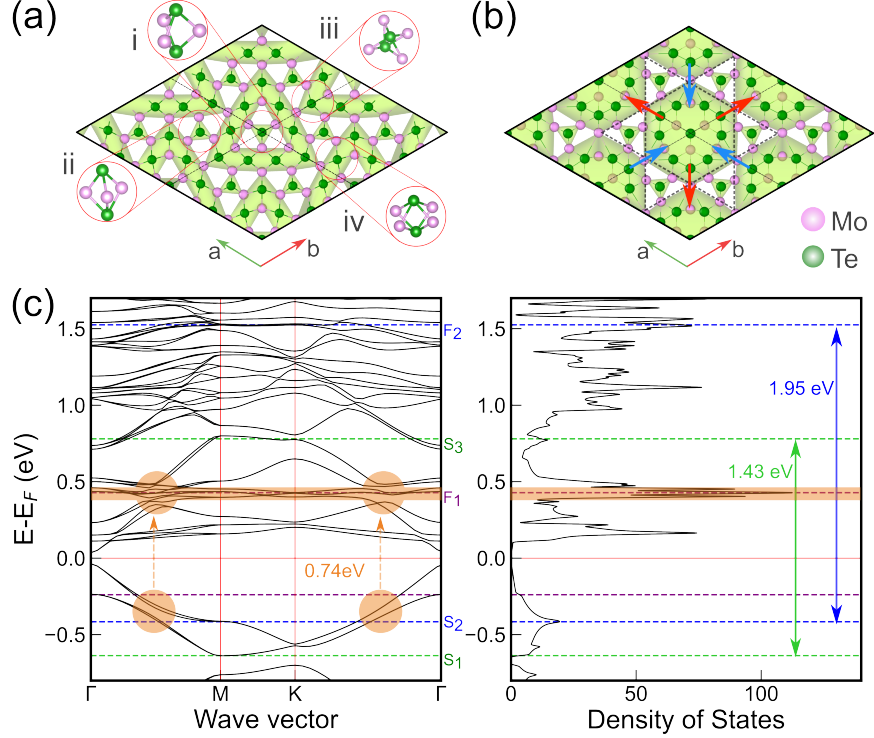


Figure 2: Geometry schematic and electronic structures of Mo_5Te_8 . (a) Crystal structure of 2×2 supercell of Mo_5Te_8 . (b) The parent ideal kagome structure for Mo_5Te_8 can be derived from (a) by moving the atoms along the arrows. (c) Energy dispersion and density of states of Mo_5Te_8 .

To further confirm the relationship between the strong shift current and the two special electronic band structures, we analyzed the density distribution of the second-order nonlinear optical conductivity. Taking the photon energy of 2.10 eV as an example, one can find that the biggest contribution of hot spots comes from the area near the M point in Figure 1g, which reflects the main contribution from the optical transition between saddle point to flat bands. Similarly, at 0.47 eV, as illustrated in Figure S3b-c, the shift current density primarily originates from six elliptical regions around the Γ point, corresponding to the optical transition from the top of the fourth band near the Γ point to the bottom of the flat bands. Therefore, the interplay between inversion symmetry breaking and two distinctive

band structures within the kagome lattice holds significant potential for generating a robust second-order nonlinear optical response.

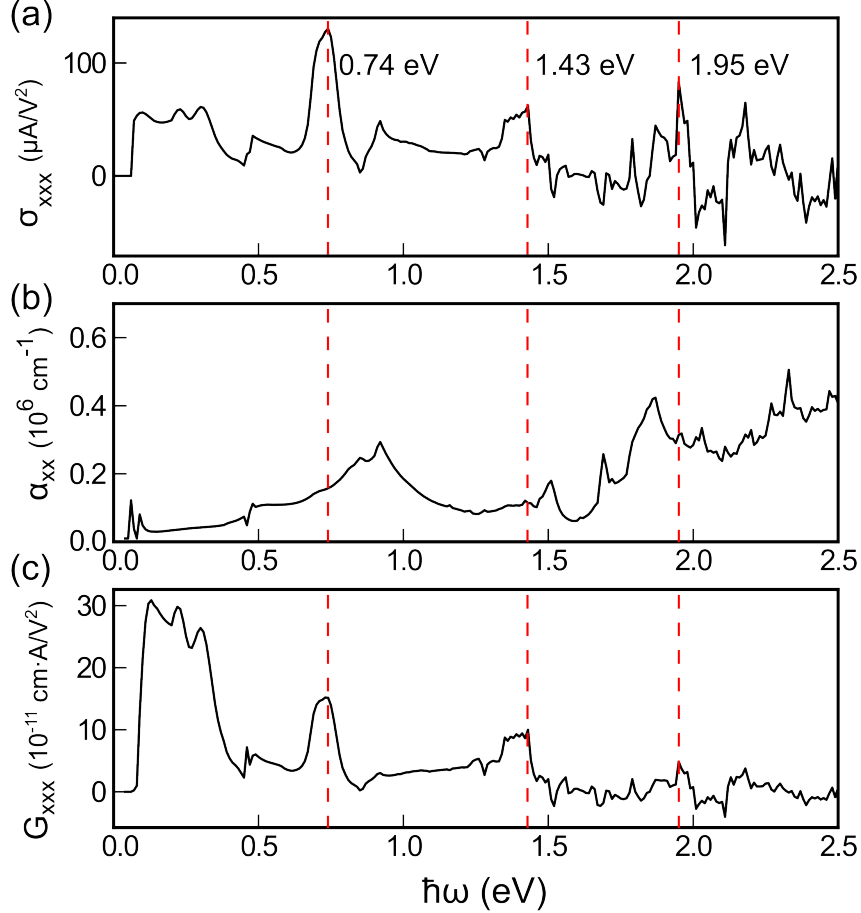


Figure 3: Optical responses in monolayer Mo_5Te_8 . (a) Shift current spectrum of σ_{xxx} tensor component, (b) absorption coefficient, and (c) Glass coefficient.

Drawing on insights from the model analysis, we now search for materials with distorted kagome lattices. Through symmetry analysis, the distorted structure in Figure 1b adopts the layer group of $P\bar{6}2m$ (No. 79). Guided by this information, we identify a synthesized material formula Mo_5Te_8 , which meets the criteria mentioned above.^{19,50} Its primitive cell consists of 15 Mo and 24 Te atoms. As illustrated in Figure 2a, a pristine 1H-MoTe₂ unit is enveloped by three uniform mirror twin boundaries (MTBs), forming a Reuleaux-triangle-shaped structural unit. When the corners of these triangles connect with the midpoints

of adjacent triangles, the overall pattern of Mo_5Te_8 emerges. This arrangement results in four distinct local atomic environments centered around Te atoms, each highlighted by a red circle in Figure 2a. The MTB regions are denser, primarily constructed of type-*iii* and type-*iv* atoms, while type-*i* and type-*ii* atoms are embedded within the framework of MTBs. Based on the highlighted MTBs region in Figure 2a and disregarding the details enclosed by the MTBs, one can identify that Mo_5Te_8 adopts a distorted kagome lattice structure accompanied by the inversion symmetry breaking. The detailed relationship between them is illustrated in Figures S1 and S7a. Naturally, Mo_5Te_8 possesses a standard kagome lattice counterpart, achievable through folding it along the six distinct directions depicted by the arrows in the Figure 2b.

The electronic band structure and DOS are depicted in Figure 2c. Since there are four types of Mo atoms in the primitive cell, and only one type forms the distorted kagome lattice, the hybridization between bands from the distorted kagome lattice and others is relatively strong. Fortunately, the features of saddle points and flat bands from Mo can still be easily recognized in the electronic band structure, as shown in Figure 2c and Figure S5-S7. Additionally, the physics near the Fermi energy is dominated by the kagome-type band structures, which are energetically separated from other occupied bands due to the presence of MTBs within its geometry. Furthermore, the band structure could be tuned through controlling the size of MTBs,⁵¹⁻⁵⁶ making Mo_5Te_8 a compelling candidate for investigating the role of the distorted kagome lattice in the bulk photovoltaic effect. Moreover, atomically thin two-dimensional materials hold significant promise as building blocks for next-generation shift current devices.⁵⁷⁻⁶¹ Therefore, Mo_5Te_8 is a potential material candidate for the study of shift current. In detail, there are four groups of flat bands near the energies of 0.16 eV, 0.43 eV, 1.10 eV, and 1.52 eV, which correspond to four prominent peaks of DOS. Moreover, four saddle points align with high-symmetry points M at energies approximately at -0.63 eV, -0.41 eV, 0.5 eV, and 0.8 eV. These points also appear as VHSs in the DOS. Therefore, Mo_5Te_8 inherits the features of kagome lattice, which could generate a large optical transition

response and hold significant potential to produce strong second-order nonlinear optical response.

Following the crystal structure of Mo_5Te_8 adopts the layer group of $P\bar{6}2m$ (No. 79), the second-order nonlinear optical conductivity tensor follows the shape of

$$\begin{bmatrix} \chi_{xxx} & -\chi_{xxx} & 0 & 0 & 0 & 0 & 0 & 0 & 0 \\ 0 & 0 & 0 & 0 & 0 & 0 & 0 & -\chi_{xxx} & -\chi_{xxx} \\ 0 & 0 & 0 & 0 & 0 & 0 & 0 & 0 & 0 \end{bmatrix} \quad (5)$$

with only one independent component χ_{xxx} , where the row index corresponds to $\{x, y, z\}$ and the column index corresponds to $\{xx, yy, zz, yz, zy, xz, zx, xy, yx\}$. The results from numerical calculations are in full agreement with the symmetry analysis. The peak value of σ_{xxx} can reach up to approximately $100 \mu\text{A}/\text{V}^2$ at the optical transition energy ~ 0.74 eV, which is a relative strong response signal,^{11,44,46,48,57,61-69} as illustrated in Figure 3a. In addition, two notable peaks near $\hbar\omega \sim 1.43$ eV and $\hbar\omega \sim 1.95$ eV are also exceed $50 \mu\text{A}/\text{V}^2$. As expected, through the optical transition energy matching, the photon energies of the three peaks above $50 \mu\text{A}/\text{V}^2$ are closely related to the optical transition involving flat bands and saddle points, as labeled in Figure 2c and Figure S6. Hence, it is clear that flat bands or saddle points play key roles in the second-order optical response of the distorted kagome lattice.

To further validate the relationship between the peak values of the second-order nonlinear optical conductivity and the band structure characteristic of the kagome lattice in Mo_5Te_8 , we depicted the conductivity density distribution by fixing the photon energies at the three peaks of the shift current. As presented in Figure 2c and Figure 4a,d, the first peak of the second-order nonlinear optical conductivity is dominated by optical transitions from a circular region near the high-symmetry point Γ to the flat bands group F_1 . In details, a bunch of flat bands near 0.45 eV collectively contribute to the shift current response at $\hbar\omega \sim 0.74$ eV and thus a relatively broader peak is present. This suggests that in real materials,

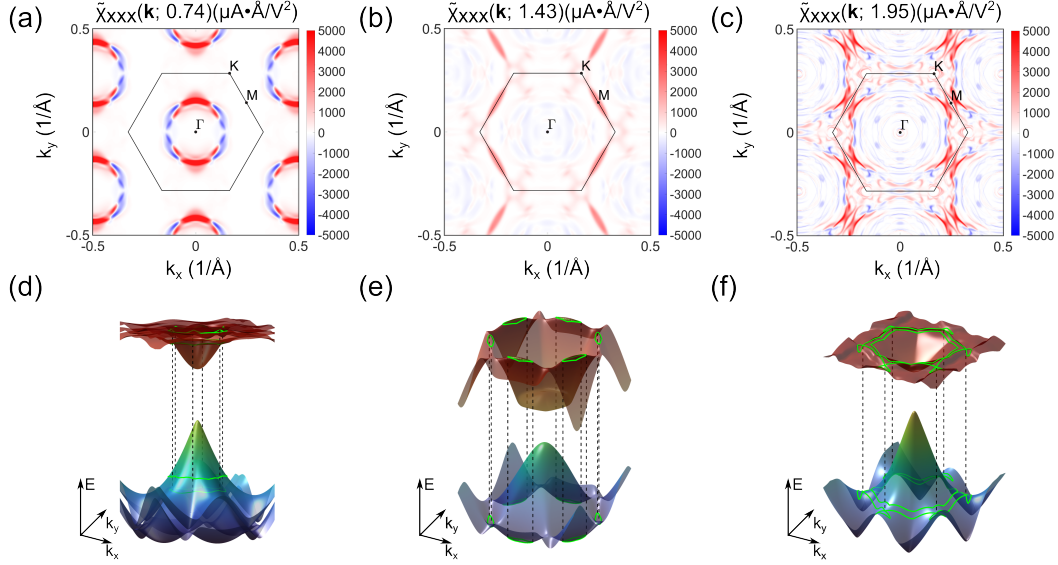


Figure 4: Relation between the second-order nonlinear optical conductivity density distribution of $\tilde{\chi}_{xxx}(\mathbf{k}; \omega)$ and electronic band structures. (a-c) The distribution of $\tilde{\chi}_{xxx}(\mathbf{k}; \omega)$ with photon energy at 0.74 eV, 1.43 eV and 1.95 eV, respectively. (d-f) Light excitation between occupied bands and non-occupied bands corresponding to (a-c).

the peak magnitude and the broadening of the optical conductivity can also be enhanced by the contribution from multiple flat bands. The peaks near $\hbar\omega \sim 1.43$ eV and $\hbar\omega \sim 1.95$ eV are mainly contributed by the optical transitions from the saddle point S_1 to the saddle point S_3 and the saddle point S_2 to the flat bands F_2 , as shown in Figures 2c and Figure 4b-c,e-f, respectively.

In the design of actual devices, optical absorption properties play a crucial role in governing the intensity of the second-order nonlinear optical response. To account for light attenuation, the intensity of the second-order nonlinear optical response is often evaluated using the Glass coefficient, defined as $G_{abb} = \frac{\sigma_{abb}(\omega)}{\alpha_{bb}(\omega)}$, where σ_{abb} is the second-order nonlinear optical conductivity and $\alpha_{bb}(\omega)$ is the absorption coefficient.^{57,62,63,70–72} As illustrated in the Figure 3b-c, the absorption coefficient and Glass coefficient of monolayer Mo_5Te_8 are provided. Notably, the Glass coefficient is on the order of $\sim 10^{-10}$ $\text{cm}\cdot\text{AV}^{-2}$, which is comparable to that of monolayer monochalcogenides.⁵⁷ Furthermore, when considering the temperature effect on the shift current response (see Figure S11), one can find that even at

300 K, only the response intensity within the frequency range of 0.3 eV is weakened, while the peak values remain largely unchanged when they lie outside this range.⁷³ Additionally, to reflect intrinsic material losses such as disorder or inelastic scattering processes, we replace the delta function by a Lorentzian in Eq. 6.⁷⁴ As shown in Figure S12, the intensity of the second-order nonlinear optical response decreases as the broadening width increases. This highlights the importance of intrinsic material losses in the design of BPVE devices.⁶⁶

To generalize our understanding of this mechanism, we extended the compound Mo_5Te_8 by substituting its elements with others from the same group in the periodic table. Drawing inspiration from the strong shift current predicted in Mo_5Te_8 , five additional counterpart compounds - W_5S_8 , Mo_5Se_8 , W_5Se_8 , Mo_5S_8 , and W_5Te_8 , were also studied. Although only Mo_5Te_8 has been experimentally synthesized thus far, we conducted calculations to evaluate the stability for the other five compounds from thermodynamically and dynamically. The results indicate that the formation energies of these compounds are negative and no imaginary phonon modes were identified^{75,76} (see Figure S4). Hence, all these five compounds are potentially stable. The calculated second-order nonlinear optical conductivity spectra are shown in Figure S10b-f, where four out of five compounds exhibit peak values exceeding $100 \mu\text{A}/\text{V}^2$, and all feature a sizeable photon energy transfer window with a value above $50 \mu\text{A}/\text{V}^2$. This suggests a general principle that the kagome lattice with inversion symmetry breaking can yield strong second-order nonlinear optical responses. Additionally, the relationship between transition energy, electronic properties, and the second-order nonlinear optical conductivity density distribution in momentum space was analyzed for each counterpart compound, as shown in Figure S8 and Figure S9. Furthermore, the effects of temperature and intrinsic material loss on the second-order nonlinear optical response are provided in Figure S11 and Figure S12, respectively. Notably, all observed cases follow the principles outlined above. Therefore, both the location of optical transition and the density distribution of the second-order nonlinear optical conductivity in momentum space confirm that shift current response in the distorted kagome lattice strongly depends on lattice-induced saddle points and flat

bands.

CONCLUSION

In summary, through effective model analysis, we demonstrated that the interplay between inversion symmetry breaking and special electronic structures of saddle points and flat bands within the kagome lattice is an effective approach to generate strong nonlinear optical response. Following this guiding principle, we have identified real materials like Mo_5Te_8 with a distorted kagome lattice that not only breaks inversion symmetry but also preserves flat bands and saddle points. The peak value of shift current in Mo_5Te_8 and its counterpart compounds can reach up to approximately $100 \mu\text{A}/\text{V}^2$. This study provides another insight into kagome lattice-related physics and materials from the perspective of the nonlinear quantum response. While our focus in this study was primarily on examining inversion symmetry breaking in the kagome lattice by rotating the triangles, we mentioned above that there are other methods can also break its inversion symmetry. We believe some of these alternative methods could yield similar effects in generating strong second-order nonlinear optical responses. This work is expected to attract further research efforts to expand the understanding of kagome lattice in the context of the second-order nonlinear optical response.

METHODS

DFT calculation details

All density functional theory (DFT) calculations presented in this work were conducted using the Vienna ab initio simulation package (VASP)^{77,78} within the Perdew-Burke-Ernzerhof (PBE)⁷⁹ generalized gradient approximation (GGA) for the exchange-correlation functional. The hybrid functional (HSE06)⁸⁰ was also employed to obtain a more accurate band structures. The projector augmented wave method was used, with a plane-wave energy cutoff of 300 eV and the \mathbf{k} -point mesh with the reciprocal space resolution of $2\pi \times 0.02 \text{ \AA}^{-1}$. For

geometry optimization, the convergence threshold for atomic force and energy is 0.01 eV/Å and 1×10^{-5} eV, respectively. To reduce the interaction effects between two adjacent layers, a vacuum layer with a width of around 15 Å was introduced in the non-periodic direction.

Calculation of the second-order nonlinear optical response

The shift current density is considered as a second-order nonlinear optical response to the electromagnetic field \mathbf{E} of frequency ω ,

$$J_a = \sigma_{abc}(0; \omega, -\omega) E_b(\omega) E_c(-\omega) \quad (6)$$

where the third-rank tensor $\sigma_{abc}(0; \omega, -\omega)$ is the shift current response tensor with Cartesian index a , b , and c . Index a denotes the direction of the generated DC current, while b and c correspond to the polarization directions of incident light.

$$\sigma_{abc}(0; \omega, -\omega) = \sum_{\mathbf{k}} \tilde{\chi}_{abc}(\mathbf{k}; \omega), \quad (7)$$

$$\tilde{\chi}_{abc}(\mathbf{k}; \omega) = \sum_{m,n} A f_{nm}^{\mathbf{k}} (r_{\mathbf{k},mn}^b r_{\mathbf{k},nm}^{c;a} + r_{\mathbf{k},mn}^c r_{\mathbf{k},nm}^{b;a}) \delta(\hbar\omega - E_{\mathbf{k},mn}), \quad (8)$$

$$r_{\mathbf{k},nm}^a = i \langle n | \partial_{k_a} | m \rangle = \frac{v_{\mathbf{k},nm}^a}{i\omega_{\mathbf{k},nm}}, \quad (9)$$

$$\begin{aligned} r_{\mathbf{k},nm}^{a;b} &= \partial_{k_b} r_{\mathbf{k},nm}^a + (\langle n | \partial_{k_b} | n \rangle - \langle m | \partial_{k_b} | m \rangle) r_{\mathbf{k},nm}^a \\ &= \frac{i}{\omega_{\mathbf{k},nm}} [v_{\mathbf{k},nm}^a \Delta_{\mathbf{k},nm}^a + v_{\mathbf{k},nm}^b \Delta_{\mathbf{k},nm}^b - \omega_{\mathbf{k},nm}^{ab} \\ &\quad + \sum_{p \neq n,m} (\frac{v_{\mathbf{k},np}^a v_{\mathbf{k},pm}^b}{\omega_{\mathbf{k},pm}} - \frac{v_{\mathbf{k},np}^b v_{\mathbf{k},pm}^a}{\omega_{\mathbf{k},np}})], \end{aligned} \quad (10)$$

where n and m are band indexes, and \mathbf{k} represents the wavevector of the Bloch wave function.

$A = \frac{ie^3\pi}{\hbar V}$ is the coefficient of shift current. $f_{nm}^k = f_n^k - f_m^k$ signifies the difference in the

Fermi-Dirac occupation numbers between band n and m , while $E_{\mathbf{k},nm} = E_{\mathbf{k},n} - E_{\mathbf{k},m}$ is the energy difference between band m and n . $v_{\mathbf{k},nm}^a = \frac{1}{\hbar} \langle n | \partial_a \hat{H} | m \rangle$ is the velocity matrix. $\Delta_{\mathbf{k},nm}^a = v_{\mathbf{k},nn}^a - v_{\mathbf{k},mm}^a$ is the difference in Fermi velocity between the band m and n , and $\omega_{\mathbf{k},nm}^{ab} = \frac{1}{\hbar} \langle n | \partial_{ab}^2 \hat{H} | m \rangle$.^{6,7,10,11,14,46}

Maximum localized Wannier function (MLWF) method was carried out to construct the tight binding models of compounds investigated in this study. This was conducted by employing the Wannier90 package⁸¹ based on the ground state results from VASP.

Shift current reported in this study was calculated using the Wannier90 package with a broadening parameter as 10 meV. To incorporate the effects of temperature and intrinsic material losses, an in-house code is employed.

The absorption coefficient is calculated with the following equation⁷¹

$$\alpha(\omega) = \sqrt{2}\omega[\sqrt{\varepsilon_1^2(\omega) + \varepsilon_2^2(\omega)} - \varepsilon_1(\omega)]^{1/2}, \quad (11)$$

where $\varepsilon_2(\omega)$ and $\varepsilon_1(\omega)$ are the real and imaginary parts of the dielectric function, respectively. The optical absorption coefficient reported in this study is calculated based on Wannier function interpolation of a hybrid density functional theory band structure.⁸²

Calculation of phonon dispersion

The phonon dispersion curves were computed using the Deep potential (DP) and phonolammps package.^{75,76} As shown in the Figure S4, the phonon dispersion results for Mo_5Te_8 obtained with DP potential agree well with that calculated using VASP. Thus, the scheme used in this study is reliable for phonon dispersion calculations.

ASSOCIATED CONTENT

Supporting Information The supporting Information is available free of charge at <https://xxx.xxx>.

Comparison between the kagome lattice and the Mo_5Te_8 lattice (Figure S1); Variation of electronic and optical properties with hopping parameters in the distorted kagome lattice (Figure S2); Electronic properties, second-order nonlinear optical conductivity density distribution, and transition energy isosurfaces of the distorted kagome lattice model (Figure S3); Phonon dispersion relations of monolayer Mo_5Te_8 , W_5S_8 , Mo_5Se_8 , W_5Se_8 , Mo_5S_8 , and W_5Te_8 (Figure S4); Weighted projected band structures of monolayer Mo_5Te_8 (Figure S5); Band structure of monolayer Mo_5Te_8 highlighting kagome-like bands near the Fermi level (Figure S6); Lattice decomposition of monolayer Mo_5Te_8 and projected band structure contributions from different Mo atoms (Figure S7); Band structures and density of states (DOS) of W_5S_8 , Mo_5Se_8 , W_5Se_8 , Mo_5S_8 , and W_5Te_8 (Figure S8); Second order nonlinear optical conductivity density distribution in momentum space (Figure S9); Shift current spectrum, absorption coefficient, and Glass coefficient of monolayer W_5S_8 , Mo_5Se_8 , W_5Se_8 , Mo_5S_8 , and W_5Te_8 (Figure S10); Temperature-dependent shift current spectrum of W_5S_8 , Mo_5Se_8 , W_5Se_8 , Mo_5S_8 , and W_5Te_8 (Figure S11); Effect of Dirac-Delta function forms and broadening parameters on the shift current spectrum of monolayer Mo_5Te_8 , W_5S_8 , Mo_5Se_8 , W_5Se_8 , Mo_5S_8 , and W_5Te_8 (Figure S12)

The tight-binding Hamiltonians are available at https://github.com/Dustglaxy/TB_files/blob/main/hr_files.tar

AUTHOR INFORMATION

Author Contributions Y.S. and X.C. conceived the idea and designed the research. X.L., J.L. and Y.S. performed the research and analyzed the data. All authors contributed to the discussion and writing of the manuscript. X.L. and J.L. contributed equally to this work.

Notes The authors declare no competing financial interest.

Acknowledgement

The authors would like to thank Ijaz Shahid and Xiliang Gong for carefully reading the manuscript. This work was supported by the Liao Ning Revitalization Talents Program (Grant No. XLYC2203080), National Natural Science Foundation of China (Grants No. 52271016, No. 52188101, and No.52422112), National Key Research and Development Program of China (Grant No. 2021YFB3501503), the National Chinese Academy of Sciences Project for Young Scientists in Basic Research (Grant No. YSBR-109), and the Special Projects of the Central Government in Guidance of Local Science and Technology Development (Grant No.2024010859-JH6/1006). Part of the calculations were carried out on the ORISE Supercomputer (Grant No. DFZX202319).

References

- (1) Ghimire, N. J.; Mazin, I. I. Topology and Correlations on the Kagome Lattice. *Nat. Mater.* **2020**, *19*, 137–138.
- (2) Kang, M.; Ye, L.; Fang, S.; You, J.-S.; Levitan, A.; Han, M.; Facio, J. I.; Jozwiak, C.; Bostwick, A.; Rotenberg, E.; Chan, M. K.; McDonald, R. D.; Graf, D.; Kaznatcheev, K.; Vescovo, E.; Bell, D. C.; Kaxiras, E.; Brink, J. v. d.; Richter, M.; Ghimire, M. P., et al. Dirac Fermions and Flat Bands in the Ideal Kagome Metal FeSn. *Nat. Mater.* **2020**, *19*, 163–169.
- (3) Neupert, T.; Denner, M. M.; Yin, J.-X.; Thomale, R.; Hasan, M. Z. Charge Order and Superconductivity in Kagome Materials. *Nat. Phys.* **2022**, *18*, 137–143.
- (4) Yin, J.-X.; Lian, B.; Hasan, M. Z. Topological Kagome Magnets and Superconductors. *Nature* **2022**, *612*, 647–657.
- (5) Wang, Y.; Wu, H.; McCandless, G. T.; Chan, J. Y.; Ali, M. N. Quantum States and Intertwining Phases in Kagome Materials. *Nat. Rev. Phys.* **2023**, *5*, 635–658.

- (6) Kraut, W.; von Baltz, R. Anomalous Bulk Photovoltaic Effect in Ferroelectrics: A Quadratic Response Theory. *Phys. Rev. B* **1979**, *19*, 1548.
- (7) von Baltz, R.; Kraut, W. Theory of the Bulk Photovoltaic Effect in Pure Crystals. *Phys. Rev. B* **1981**, *23*, 5590.
- (8) Campi, D.; Coli, G.; Vallone, M. Formulation of the Optical Response in Semiconductors and Quantum-Confined Structures. *Phys. Rev. B* **1998**, *57*, 4681.
- (9) Orapunt, F.; O’Leary, S. K. Optical Transitions and the Mobility Edge in Amorphous Semiconductors: A Joint Density of States Analysis. *J. Appl. Phys.* **2008**, *104*, 073513.
- (10) Xiao, D.; Chang, M.-C.; Niu, Q. Berry Phase Effects on Electronic Properties. *Rev. Mod. Phys.* **2010**, *82*, 1959–2007.
- (11) Young, S. M.; Rappe, A. M. First Principles Calculation of the Shift Current Photovoltaic Effect in Ferroelectrics. *Phys. Rev. Lett.* **2012**, *109*, 116601.
- (12) Tan, L. Z.; Rappe, A. M. Enhancement of the Bulk Photovoltaic Effect in Topological Insulators. *Phys. Rev. Lett.* **2016**, *116*, 237402.
- (13) Gupta, S.; Shirodkar, S. N.; Kutana, A.; Yakobson, B. I. In Pursuit of 2D Materials for Maximum Optical Response. *ACS Nano* **2018**, *12*, 10880–10889.
- (14) Qian, Z.; Zhou, J.; Wang, H.; Liu, S. Shift Current Response in Elemental Two-Dimensional Ferroelectrics. *npj Comput. Mater.* **2023**, *9*, 67.
- (15) You, J.-Y.; Su, G.; Feng, Y. P. A Versatile Model with Three-Dimensional Triangular Lattice for Unconventional Transport and Various Topological Effects. *Natl. Sci. Rev.* **2024**, *11*, nwad114.
- (16) Tanaka, H.; Watanabe, H.; Yanase, Y. Nonlinear Optical Response in Superconductors in Magnetic Field: Quantum Geometry and Topological Superconductivity. *Phys. Rev. B* **2024**, *110*, 014520.

- (17) Lai, J.; Zhan, J.; Liu, P.; Shirakawa, T.; Seiji, Y.; Chen, X.-Q.; Sun, Y. Universal Enhancement Effect of Nonlinear Optical Response From Band Hybridization. *Adv. Opt. Mater.* **2021**, *13*, 2401143.
- (18) Chen, Z.; Fang, Y.; Cheng, M.; Lü, T.-Y.; Cao, X.; Zhu, Z.-Z.; Wu, S. Large Second-Harmonic Generation and Linear Electro-Optic Effect in the Bulk Kagome Lattice Compound Nb_3MX_7 (M= Se, S, Te; X= I, Br). *Phy. Rev. B* **2024**, *109*, 115118.
- (19) Zhang, J.; Xia, Y.; Wang, B.; Jin, Y.; Tian, H.; Kin Ho, W.; Xu, H.; Jin, C.; Xie, M. Single-Layer Mo_5Te_8 —A New Polymorph of Layered Transition-Metal Chalcogenide. *2D Mater.* **2020**, *8*, 015006.
- (20) Wang, Y.; Bobev, S. Synthesis and Crystal Structure of the Zintl Phases NaSrSb , NaBaSb and NaEuSb . *Materials* **2023**, *16*, 1428.
- (21) Iandelli, A.; Franceschi, E. On the Crystal Structure of the Compounds CaP , SrP , CaAs , SrAs and EuAs . *J. Less Common Met.* **1973**, *30*, 211–216.
- (22) Zhuravlev, Y. N.; Obolonskaya, O. Structure, Mechanical Stability, and Chemical Bond in Alkali Metal Oxides. *J. Struct. Chem.* **2010**, *51*, 1005–1013.
- (23) Duan, S.; You, J.-Y.; Cai, Z.; Gou, J.; Li, D.; Huang, Y. L.; Yu, X.; Teo, S. L.; Sun, S.; Wang, Y., et al. Observation of Kagome-Like Bands in Two-Dimensional Semiconducting $\text{Cr}_8\text{Se}_{12}$. *Nat. Commun.* **2024**, *15*, 8940.
- (24) Xie, Y.; Ji, K.; He, J.; Shen, X.; Wang, D.; Zhang, J. Manipulation of Topology by Electric Field in Breathing Kagome Lattice. *arXiv* **2024**, 2411.17208, DOI:10.48550/arXiv.2411.17208.
- (25) Du, L.; Hasan, T.; Castellanos-Gomez, A.; Liu, G.-B.; Yao, Y.; Lau, C. N.; Sun, Z. Engineering Symmetry Breaking in 2D Layered Materials. *Nat. Rev. Phys.* **2021**, *3*, 193–206.

- (26) Zhou, H.; dos Santos Dias, M.; Zhang, Y.; Zhao, W.; Lounis, S. Kagomerization of Transition Metal Monolayers Induced by Two-Dimensional Hexagonal Boron Nitride. *Nat. Commun.* **2024**, *15*, 4854.
- (27) Deng, J.; Guo, D.; Wen, Y.; Lu, S.; Zhang, H.; Cheng, Z.; Pan, Z.; Jian, T.; Li, D.; Wang, H.; Bai, Y.; Li, Z.; Ji, W.; He, j.; Zhang, C. Evidence of Ferroelectricity in an Antiferromagnetic Vanadium Trichloride Monolayer. *Science Advances* **2025**, *11*, eado6538.
- (28) Lee, J. H.; Kim, G. W.; Song, I.; Kim, Y.; Lee, Y.; Yoo, S. J.; Cho, D.-Y.; Rhim, J.-W.; Jung, J.; Kim, G.; Kim, C. Atomically Thin Two-Dimensional Kagome Flat Band on the Silicon Surface. *ACS nano* **2024**, *18*, 25535–25541.
- (29) Li, Y.; Zhai, S.; Liu, Y.; Zhang, J.; Meng, Z.; Zhuang, J.; Feng, H.; Xu, X.; Hao, W.; Zhou, M.; Lu, G.-H.; Dou, S.; Du, Y. Electronic Flat Band in Distorted Colouring Triangle Lattice. *Adv. Sci.* **2024**, *11*, 2303483.
- (30) Liu, C.; Chang, T.; Wang, S.; Zhou, S.; Wang, X.; Fan, C.; Han, L.; Li, F.; Ren, H.; Wang, S.; Chen, Y.-S.; Zhang, J. Cascade of Phase Transitions and Large Magnetic Anisotropy in a Triangle-Kagome-Triangle Trilayer Antiferromagnet. *Chem. Mater.* **2024**, *36*, 9516–9525.
- (31) Wang, Y.; McCandless, G. T.; Wang, X.; Thanabalasingam, K.; Wu, H.; Bouwmeester, D.; Van Der Zant, H. S.; Ali, M. N.; Chan, J. Y. Electronic Properties and Phase Transition in the Kagome Metal $\text{Yb}_{0.5}\text{Co}_3\text{Ge}_3$. *Chem. Mater.* **2022**, *34*, 7337–7343.
- (32) Wu, S.; Klemm, M. L.; Shah, J.; Ritz, E. T.; Duan, C.; Teng, X.; Gao, B.; Ye, F.; Matsuda, M.; Li, F.; Xu, X.; Yi, M.; Birol, T.; Dai, P.; Blumberg, G. Symmetry Breaking and Ascending in the Magnetic Kagome Metal FeGe. *Phys. Rev. X* **2024**, *14*, 011043.

- (33) Li, H.; Yu, X.; Shen, X.; Tang, G.; Han, K. External Electric Field Induced Second-Order Nonlinear Optical Effects in Hexagonal Graphene Quantum Dots. *J. Phys. Chem. C* **2019**, *123*, 20020–20025.
- (34) Jiang, J.; Chen, Z.; Hu, Y.; Xiang, Y.; Zhang, L.; Wang, Y.; Wang, G.-C.; Shi, J. Flexo-Photovoltaic Effect in MoS₂. *Nat. Nanotechnol.* **2021**, *16*, 894–901.
- (35) Zhang, H.; Oli, B. D.; Zou, Q.; Guo, X.; Wang, Z.; Li, L. Visualizing Symmetry-Breaking Electronic Orders in Epitaxial Kagome Magnet FeSn Films. *Nat. Commun.* **2023**, *14*, 6167.
- (36) Zeng, G.; Zhang, R.; Sui, Y.; Li, X.; OuYang, H.; Pu, M.; Chen, H.; Ma, X.; Cheng, X.; Yan, W.; Xu, M.; Hong, M. Inversion Symmetry Breaking in Lithium Intercalated Graphitic Materials. *ACS Applied Materials & Interfaces* **2020**, *12*, 28561–28567.
- (37) Wu, Q.; Quan, W.; Pan, S.; Hu, J.; Zhang, Z.; Wang, J.; Zheng, F.; Zhang, Y. Atomically Thin Kagome-Structured Co₉Te₁₆ Achieved Through Self-Intercalation and Its Flat Band Visualization. *Nano Lett.* **2024**, *24*, 7672–7680.
- (38) Jo, J.; Kim, J. H.; Kim, C. H.; Lee, J.; Choe, D.; Oh, I.; Lee, S.; Lee, Z.; Jin, H.; Yoo, J.-W. Defect-Gradient-Induced Rashba Effect in Van Der Waals PtSe₂ Layers. *Nat. Commun.* **2022**, *13*, 2759.
- (39) Mu, X.; Xue, Q.; Sun, Y.; Zhou, J. Magnetic Proximity Enabled Bulk Photovoltaic Effects in Van Der Waals Heterostructures. *Phys. Rev. Res.* **2023**, *5*, 013001.
- (40) Gao, Q.; Yan, Q.; Hu, Z.; Chen, L. Bilayer Kagome Borophene with Multiple Van Hove Singularities. *Adv. Sci.* **2024**, *11*, 2305059.
- (41) Ziman, J. *Solid State Physics*; Elsevier, 1971; Vol. 26; pp 1–101.
- (42) Anderson, J. M.; Clunie, J.; Pommerenke, C. On Bloch Functions and Normal Functions. *J. Reine Angew. Math.* **1974**, *270*, 12–37.

- (43) Beugeling, W.; Everts, J.; Morais Smith, C. Topological Phase Transitions Driven by Next-Nearest-Neighbor Hopping in Two-Dimensional Lattices. *Phys. Rev. B* **2012**, *86*, 195129.
- (44) Cook, A. M.; M. Fregoso, B.; De Juan, F.; Coh, S.; Moore, J. E. Design Principles for Shift Current Photovoltaics. *Nat. Commun.* **2017**, *8*, 14176.
- (45) Zhang, S.; Kang, M.; Huang, H.; Jiang, W.; Ni, X.; Kang, L.; Zhang, S.; Xu, H.; Liu, Z.; Liu, F. Kagome Bands Disguised in a Coloring-Triangle Lattice. *Phys. Rev. B* **2019**, *99*, 100404.
- (46) Ibañez-Azpiroz, J.; Tsirkin, S. S.; Souza, I. Ab Initio Calculation of the Shift Photocurrent by Wannier Interpolation. *Phys. Rev. B* **2018**, *97*, 245143.
- (47) Zhang, Y.; Ideue, T.; Onga, M.; Qin, F.; Suzuki, R.; Zak, A.; Tenne, R.; Smet, J.; Iwasa, Y. Enhanced Intrinsic Photovoltaic Effect in Tungsten Disulfide Nanotubes. *Nature* **2019**, *570*, 349–353.
- (48) Sauer, M. O.; Taghizadeh, A.; Petralanda, U.; Ovesen, M.; Thygesen, K. S.; Olsen, T.; Cornean, H.; Pedersen, T. G. Shift Current Photovoltaic Efficiency of 2D Materials. *npj Comput. Mater.* **2023**, *9*, 35.
- (49) Liang, Z.; Zhou, X.; Zhang, L.; Yu, X.-L.; Lv, Y.; Song, X.; Zhou, Y.; Wang, H.; Wang, S.; Wang, T.; Shum, P. P.; He, Q.; Liu, Y.; Zhu, C.; Wang, L.; Chen, X. Strong Bulk Photovoltaic Effect in Engineered Edge-Embedded Van Der Waals Structures. *Nat. Commun.* **2023**, *14*, 4230.
- (50) Lei, L.; Dai, J.; Dong, H.; Geng, Y.; Cao, F.; Wang, C.; Xu, R.; Pang, F.; Liu, Z.-X.; Li, F.; Cheng, Z.; Wang, G.; Ji, W. Electronic Janus Lattice and Kagome-Like Bands in Coloring-Triangular MoTe₂ Monolayers. *Nat. Commun.* **2023**, *14*, 6320.

- (51) Tan, L. Z.; Zheng, F.; Young, S. M.; Wang, F.; Liu, S.; Rappe, A. M. Shift Current Bulk Photovoltaic Effect in Polar Materials—Hybrid and Oxide Perovskites and Beyond. *npj Comput. Mater.* **2016**, *2*, 16026.
- (52) Bihari Swain, A.; Murali, D.; Nanda, B.; Murugavel, P. Large Bulk Photovoltaic Response by Symmetry-Breaking Structural Transformation in Ferroelectric $[\text{Ba}(\text{Zr}_{0.2}\text{Ti}_{0.8})\text{O}_3]_{0.5}[(\text{Ba}_{0.7}\text{Ca}_{0.3})\text{TiO}_3]_{0.5}$. *Phys. Rev. Appl.* **2019**, *11*, 044007.
- (53) Tan, L. Z.; Rappe, A. M. Upper Limit on Shift Current Generation in Extended Systems. *Phys. Rev. B* **2019**, *100*, 085102.
- (54) Dai, J.; Zhang, Z.; Pan, Z.; Wang, C.; Zhang, C.; Cheng, Z.; Ji, W. Kagome Bands and Magnetism in MoTe_{2-x} Kagome Monolayers. *arXiv* **2024**, 2408.14285, DOI:[10.48550/arXiv.2408.14285](https://doi.org/10.48550/arXiv.2408.14285).
- (55) Hong, J.; Wang, C.; Liu, H.; Ren, X.; Chen, J.; Wang, G.; Jia, J.; Xie, M.; Jin, C.; Ji, W.; Yuan, J.; Zhang, Z. Inversion Domain Boundary Induced Stacking and Bandstructure Diversity in Bilayer MoSe_2 . *Nano Lett.* **2017**, *17*, 6653–6660.
- (56) Liu, H.; Jiao, L.; Yang, F.; Cai, Y.; Wu, X.; Ho, W.; Gao, C.; Jia, J.; Wang, N.; Fan, H.; Yao, W.; Xie, M. Dense Network of One-Dimensional Midgap Metallic Modes in Monolayer MoSe_2 and Their Spatial Undulations. *Phys. Rev. Lett.* **2014**, *113*, 066105.
- (57) Rangel, T.; Fregoso, B. M.; Mendoza, B. S.; Morimoto, T.; Moore, J. E.; Neaton, J. B. Large Bulk Photovoltaic Effect and Spontaneous Polarization of Single-Layer Monochalcogenides. *Phys. Rev. Lett.* **2017**, *119*, 067402.
- (58) Chan, Y.-H.; Qiu, D. Y.; da Jornada, F. H.; Louie, S. G. Giant Exciton-Enhanced Shift Currents and Direct Current Conduction with Subbandgap Photo Excitations Produced by Many-Electron Interactions. *Proc. Natl. Acad. Sci.* **2021**, *118*, e1906938118.

- (59) Xu, H.; Wang, H.; Zhou, J.; Guo, Y.; Kong, J.; Li, J. Colossal Switchable Photocurrents in Topological Janus Transition Metal Dichalcogenides. *npj Comput. Mater.* **2021**, *7*, 31.
- (60) Xiao, R.-C.; Gao, Y.; Jiang, H.; Gan, W.; Zhang, C.; Li, H. Non-Synchronous Bulk Photovoltaic Effect in Two-Dimensional Interlayer-Sliding Ferroelectrics. *npj Comput. Mater.* **2022**, *8*, 138.
- (61) Jin, G.; He, L. Peculiar Band Geometry Induced Giant Shift Current in Ferroelectric SnTe Monolayer. *npj Comput. Mater.* **2024**, *10*, 23.
- (62) Young, S. M.; Zheng, F.; Rappe, A. M. First-Principles Calculation of the Bulk Photovoltaic Effect in Bismuth Ferrite. *Phys. Rev. Lett.* **2012**, *109*, 236601.
- (63) Brehm, J. A.; Young, S. M.; Zheng, F.; Rappe, A. M. First-Principles Calculation of the Bulk Photovoltaic Effect in the Polar Compounds LiAsS₂, LiAsSe₂, and NaAsSe₂. *J. Chem. Phys.* **2014**, *141*, 204704.
- (64) Wang, C.; Liu, X.; Kang, L.; Gu, B.-L.; Xu, Y.; Duan, W. First-Principles Calculation of Nonlinear Optical Responses by Wannier Interpolation. *Phys. Rev. B* **2017**, *96*, 115147.
- (65) Zhang, Y.; Holder, T.; Ishizuka, H.; de Juan, F.; Nagaosa, N.; Felser, C.; Yan, B. Switchable Magnetic Bulk Photovoltaic Effect in the Two-Dimensional Magnet CrI₃. *Nat. Commun.* **2019**, *10*, 3783.
- (66) Sotome, M.; Nakamura, M.; Fujioka, J.; Ogino, M.; Kaneko, Y.; Morimoto, T.; Zhang, Y.; Kawasaki, M.; Nagaosa, N.; Tokura, Y.; Ogawa, N. Spectral Dynamics of Shift Current in Ferroelectric Semiconductor SbSi. *Proc. Natl. Acad. Sci.* **2019**, *116*, 1929–1933.

- (67) Chan, Y.-H.; Qiu, D. Y.; da Jornada, F. H.; Louie, S. G. Exciton Shift Currents: DC Conduction with Sub-Bandgap Photo Excitations. *arXiv* **2019**, 1904.12813, DOI:[10.48550/arXiv.1904.12813](https://doi.org/10.48550/arXiv.1904.12813).
- (68) Fei, R.; Tan, L. Z.; Rappe, A. M. Shift-Current Bulk Photovoltaic Effect Influenced by Quasiparticle and Exciton. *Phys. Rev. B* **2020**, *101*, 045104.
- (69) Schankler, A. M.; Gao, L.; Rappe, A. M. Large Bulk Piezophotovoltaic Effect of Monolayer 2H-MoS₂. *J. Phys. Chem. Lett.* **2021**, *12*, 1244–1249.
- (70) Glass, A.; Linde, D. v. d.; Negran, T. In *Landmark papers on photorefractive nonlinear optics*; Pochi, Y., Gu, C., Eds.; World Scientific, 1995; pp 371–373.
- (71) Lalitha, S.; Karazhanov, S. Z.; Ravindran, P.; Senthilarasu, S.; Sathyamoorthy, R.; Janabergenov, J. Electronic Structure, Structural and Optical Properties of Thermally Evaporated CdTe Thin Films. *Physica B* **2007**, *387*, 227–238.
- (72) Ma, Q.; Grushin, A. G.; Burch, K. S. Topology and Geometry Under the Nonlinear Electromagnetic Spotlight. *Nat. Mater.* **2021**, *20*, 1601–1614.
- (73) Yang, X.; Burch, K.; Ran, Y. Divergent Bulk Photovoltaic Effect in Weyl Semimetals. *arXiv* **2017**, 1712.09363, DOI:[10.48550/arXiv.1712.09363](https://doi.org/10.48550/arXiv.1712.09363).
- (74) Chaubey, M. P.; Van Vliet, C. M. Transverse Magnetoconductivity of Quasi-Two-Dimensional Semiconductor Layers in the Presence of Phonon Scattering. *Phys. Rev. B* **1986**, *33*, 5617.
- (75) Togo, A.; Tanaka, I. First Principles Phonon Calculations in Materials Science. *Scr. Mater.* **2015**, *108*, 1–5.
- (76) Carreras, A. A Phonolammps: A Python Interface for LAMMPS Phonon Calculations Using Phonopy. **2020**, *Zenodo* <https://doi.org/10.5281/zenodo.3940626>.

- (77) Kresse, G.; Furthmüller, J. Efficient Iterative Schemes for Ab Initio Total-Energy Calculations Using a Plane-Wave Basis Set. *Phys. Rev. B* **1996**, *54*, 11169.
- (78) Kresse, G.; Furthmüller, J. Efficiency of Ab-Initio Total Energy Calculations for Metals and Semiconductors Using a Plane-Wave Basis Set. *Comput. Mater. Sci.* **1996**, *6*, 15–50.
- (79) Ernzerhof, M.; Scuseria, G. E. Assessment of the Perdew–Burke–Ernzerhof Exchange–Correlation Functional. *J. Chem. Phys.* **1999**, *110*, 5029–5036.
- (80) Krukau, A. V.; Vydrov, O. A.; Izmaylov, A. F.; Scuseria, G. E. Influence of the Exchange Screening Parameter on the Performance of Screened Hybrid Functionals. *J. Chem. Phys.* **2006**, *125*, 224106.
- (81) Mostofi, A. A.; Yates, J. R.; Lee, Y.-S.; Souza, I.; Vanderbilt, D.; Marzari, N. Wannier90: A Tool for Obtaining Maximally-Localised Wannier Functions. *Comput. Phys. Commun.* **2008**, *178*, 685–699.
- (82) Kim, S.; Walsh, A. Ab Initio Calculation of the Detailed Balance Limit to the Photovoltaic Efficiency of Single P-N Junction Kesterite Solar Cells. *Appl. Phys. Lett.* **2021**, *118*, 243905.